



Janus Hollow Nanofiber with Bifunctional Oxygen Electrocatalyst for Rechargeable Zn-Air Battery

Chen, Xing; Pu, Jie; Hu, Xuhui; Yao, Yuechao; Dou, Yibo; Jiang, Jianjun; Zhang, Wenjing

Published in:
Small

Link to article, DOI:
[10.1002/sml.202200578](https://doi.org/10.1002/sml.202200578)

Publication date:
2022

Document Version
Publisher's PDF, also known as Version of record

[Link back to DTU Orbit](#)

Citation (APA):
Chen, X., Pu, J., Hu, X., Yao, Y., Dou, Y., Jiang, J., & Zhang, W. (2022). Janus Hollow Nanofiber with Bifunctional Oxygen Electrocatalyst for Rechargeable Zn-Air Battery. *Small*, 18(16), Article 2200578. <https://doi.org/10.1002/sml.202200578>

General rights

Copyright and moral rights for the publications made accessible in the public portal are retained by the authors and/or other copyright owners and it is a condition of accessing publications that users recognise and abide by the legal requirements associated with these rights.

- Users may download and print one copy of any publication from the public portal for the purpose of private study or research.
- You may not further distribute the material or use it for any profit-making activity or commercial gain
- You may freely distribute the URL identifying the publication in the public portal

If you believe that this document breaches copyright please contact us providing details, and we will remove access to the work immediately and investigate your claim.

Janus Hollow Nanofiber with Bifunctional Oxygen Electrocatalyst for Rechargeable Zn–Air Battery

Xing Chen, Jie Pu, Xuhui Hu, Yuechao Yao, Yibo Dou, Jianjun Jiang,*
and Wenjing Zhang*

Zn–air battery technologies have received increasing attention, while the application is hindered by the sluggish kinetics of the oxygen evolution reaction (OER) and oxygen reduction reaction (ORR). In order to explore an efficient method to fabricate a high-performance electrocatalyst via modification of advanced nanostructure, a coaxial electrospinning method with in-situ synthesis and subsequent carbonization to construct 3D flexible Janus-like electrocatalysts is developed. The resulting Janus nanofibers have a unique core–shell hollow fiber structure, where NiFe alloy electrocatalysts supported by N-doped carbon nanobelt are located on the inner wall of the carbon layer, and leaf-like Co–N nanosheets are anchored on the outer wall of the carbon layer. As a result, the electrocatalyst exhibits excellent bifunctional catalytic performance for ORR and OER, demonstrating the small potential gap value of 0.73 V between the ORR half-wave potential and the OER potential at 10 mA cm⁻², which is even comparable to the mixed commercial noble catalyst with 20% Pt/C and RuO₂. The rechargeable Zn–air battery is constructed and displays a large open-circuit voltage of 1.44 V, high power density (130 mW cm⁻²) and energy density (874 Wh kg⁻¹). This study provides a concept to synthesize and construct high performance bifunctional electrocatalysts.

1. Introduction

With the rapid development of the economy, the increasing demand for environment-friendly and renewable energy have attracted extensive attention.^[1–3] Among various energy storage and conversion system, the rechargeable zinc–air battery has received great attention because of its high theoretical energy density, low cost, and high safety.^[4] However, the sluggish reaction kinetics of reversible oxygen reactions inhibits the potential application. In order to tackle this challenge, the charge and discharge process of zinc–air batteries corresponding to the oxygen evolution reaction (OER) and the oxygen reduction reaction (ORR) should be optimized by the efficient bifunctional electrocatalysts to reduce the energy barriers.^[5,6] Noble metal electrocatalysts, such as Pt-based and Ru-/Ir-based materials, are the state-of-the-art ORR and OER electrocatalysts, while the high cost and the natural scarcity with poor stability hamper their

large-scale applications. Therefore, the rational design of effective bifunctional electrocatalysts with low-cost but high stability is a challenging and urgent task.


To date, research efforts have been devoted to designing nonprecious metal catalysts, such as carbon-based materials, transition-metal oxides, metal alloy, and heteroatoms doped materials.^[7–10] Among the categories, metal–nitrogen–carbon (M–N–C) materials serve as promising candidates with desirable performance to reduce the overall cost and enhance the stability of Pt-/Ru-based electrocatalysts. The nitrogen atoms anchor metal species and play an essential role in regulating the electronic structures of the electrocatalysts.^[11] In such encapsulated structures, the thin carbon shell could prevent direct contact with electrolyte and metal nanoparticles, contributing to long-term stability.^[12] In turn, the work function difference between the carbon shell and the metal atoms will promote the electron transfer from metal atoms to the carbon surface, leading to the decrease of local work function on the carbon surface and the increase of the density of states (DOS) near Fermi level on the carbon surface. The decreased local work function could decrease the free energy of the intermediates and improve the electrocatalytic activity.^[13,14] With this concept in mind, extensive research has been focused on constructing the M–C–N-based catalysts. For example, the

X. Chen, J. Jiang
School of Mechanical Engineering
Northwestern Polytechnical University
Xi'an 710072, P. R. China
E-mail: jianjun@nwpu.edu.cn

X. Chen, Y. Yao, W. Zhang
Department of Environmental Engineering
Technical University of Denmark
Miljøvej 113, Kgs. Lyngby 2800, Denmark
E-mail: wenz@dtu.dk

J. Pu
Frontiers Science Center for Flexible Electronics
Institute of Flexible Electronics
Northwestern Polytechnical University
Xi'an 710072, P. R. China

X. Hu, Y. Dou
State Key Laboratory of Chemical Resource Engineering
Beijing University of Chemical Technology
Beijing 100029, P. R. China

 The ORCID identification number(s) for the author(s) of this article can be found under <https://doi.org/10.1002/smll.202200578>.

© 2022 The Authors. Small published by Wiley-VCH GmbH. This is an open access article under the terms of the Creative Commons Attribution-NonCommercial-NoDerivs License, which permits use and distribution in any medium, provided the original work is properly cited, the use is non-commercial and no modifications or adaptations are made.

DOI: 10.1002/smll.202200578

Co–N–C electrocatalysts were recently reported, which showed remarkable ORR activity.^[15–17] Co, N-codoped carbon nanoframes displayed an ORR half-wave potential of 0.79 V.^[18] Atomically dispersed Co–N exhibited a more positive potential of 0.91 V than that of the benchmark of Pt/C,^[19] and the introduction of defects on Co–N–C could improve the intrinsic activity of atomic metal catalyst.^[20] The MOF derived Co–N showed a half-wave potential of 0.89 V, and the density-functional theory (DFT) result confirmed that CoN₄ was more active than that of other CoN_x configurations ($x = 1 - 3$).^[21] Nevertheless, many Co–N–C composites cannot fulfil the practical application of rechargeable zinc–air batteries because of their large potential gap as bifunctional electrocatalysts. The reason is the large free energy difference between HOO* and HO* leading to the poor OER activity, even though Co–N–C composites exhibited favorable OH* adsorption and OOH* desorption capabilities.^[2,21]

Recently, nitrogen-doped carbon decorated with NiFe alloy has been introduced as a promising strategy for the fabrication of bifunctional electrocatalysts. NiFe–N–C nanosheets and NiFe@N carbon nanotubes with outstanding electrocatalytic performance have been reported. The bifunctional NiFe nanoparticles embedded in N-doped carbon tubes exhibited a low overpotential of 290 mV at 10 mA cm⁻² for OER, and a half-wave potential of 0.75 mV for ORR.^[22] The NiFe nanoparticles covered with N-doped carbon sheets exhibited an overpotential of 370 mV at 10 mA cm⁻², and a half-wave potential of 0.84 mV.^[23] A composite of NiFe alloy nanoparticles embedded in N-doped bamboo-like carbon nanotubes exhibited a OER activity (195 mV at 10 mA cm⁻²) and a ORR activity (half-wave potential of 0.83 V).^[24] Unlike the Co–N–C structure, the Ni–Fe–N–C bimetallic materials own superior activity for OER but limited ORR performance. Previous DFT results confirmed that Ni–Fe–N–C bimetallic materials endowed a small free energy difference between HOO* and HO*, leading to the pronounced OER activity, while a large free energy difference between HOO* and O₂ leading to the poor ORR activity.^[2] With the aforementioned synthesized considerations, the use of M–N–C compounds to catalyze both OER and ORR represents a promising approach. Despite the substantial research on a rational structure design and composition optimization, the inherent potential gap of Co-/NiFe-based materials is limited to reducing the energy barriers. Therefore, it is still a huge challenge to construct the high efficient and low-cost bifunctional electrocatalysts for Zn–air batteries.

Janus materials feature asymmetric properties on two opposing sides, bringing new opportunities to design novel bifunctional materials that the conventional approaches could not achieve. Since the “Janus” concept was proposed by de Gennes in 1991,^[25] numerous Janus structures, such as sheets, rods, spheres, and membranes, have been precisely designed for bifunctional catalysts, switchable ion transport and multifunctional sensor.^[5,26–28] With the aforementioned synthesized considerations, the Co–N–C structure showed excellent ORR performance but limited OER activity. On the contrary, the NiFe–N–C structure exhibited superior OER activity but restricted ORR performance. The unique Janus structures with different properties provide a possible approach to construct a Janus electrocatalyst with selective oxygen electrocatalysts, while

it is still tricky to synthesize the flexible 3D Janus oxygen electrocatalysts satisfying the above critical challenges. Electrospinning is a versatile technique to fabricate continuous nanofibers and possesses many favorable properties such as high porosity and continuous ion-conducting pathways, making the electrospun nanofibers a promising material to construct 3D electrodes for various energy storage applications.^[29,30] In general, electrospun carbon fibers decorated with metal nanoparticles have been reported.^[31] Meanwhile, to obtain a bifunctional electrocatalyst, researchers have designed a composite structure where in situ growth synthesis was used to introduce another electrocatalyst with different properties on the synthesized solid nanofibers.^[32] As an alternative route, the desired bifunctional electrocatalysts were constructed by introducing various metal salt in the electrospun solutions.^[29,33] However, the nanoparticles embedded in fibers had limited active sites, thus reducing the electrocatalysts performance.

Herein, a novel and scalable fabrication strategy was developed to construct 3D flexible Janus hollow nanofibers with excellent bifunctional electrocatalytic activity by applying coaxial electrospinning and in situ growth techniques. The resulting materials are composed of two different functional catalysts separated by the thin-walled carbon layer. The structure and morphology of Janus nanofibers can be precisely regulated by altering the synthesis conditions. Its inner layer is comprised of NiFe alloy nanoparticles embedded in an N-doped nanobelt (Ni–Fe–N–C) as a super electrocatalyst for OER. The middle layer is composed of conductive thin-walled carbon, playing a dual role of a current collector and a 3D framework to support functional materials. The outer layer is constituted of leaf-like Co–N–C with highly opened nanoporous structures and high exposed active sites, which is active for ORR. Benefiting from this unique Janus structure, the synthesized flexible Ni–Fe–N–C@C@Co–N–C carbon nanofibers (denoted as NiFe@C@Co CNFs) exhibit remarkable OER/ORR catalytic performance. As a result, the rechargeable Zn–air battery using NiFe@C@Co CNFs as electrode shows an excellent power density and stability.

2. Results

The multistep preparation strategy for NiFe@C@Co carbon nanofiber is shown in **Figure 1**. First, the coaxial electrospinning technology was used to obtain 1D core–shell polymer fiber, in which poly(methyl methacrylate) (PMMA)/polyacrylonitrile (PAN)/Ni(Ac)₂/Fe(AcAc)₃ were chosen as the inner solution, and PAN was chosen as the outer solution (denoted as NiFe@PAN PF). The complex inner solution in core–shell fiber can be attributed to three main factors: i) PMMA, due to lower degradation temperature as compared to PAN, is used as a sacrifice template to yield a hollow structure. ii) PAN is used as the precursor to form nitrogen-doped carbon and M (Fe, Ni, Co)–N–C structure. iii) PAN is employed to improve the flexibility and charge transfer and is the key carbon source to wrap metal nanoparticles and anchor NiFe alloy on the inner wall of the hollow carbon layer. iv) PMMA and PAN with insoluble nature maintain the solid fiber structure during in situ growth process, which ensures ZIF-L are grown on the fiber surface.

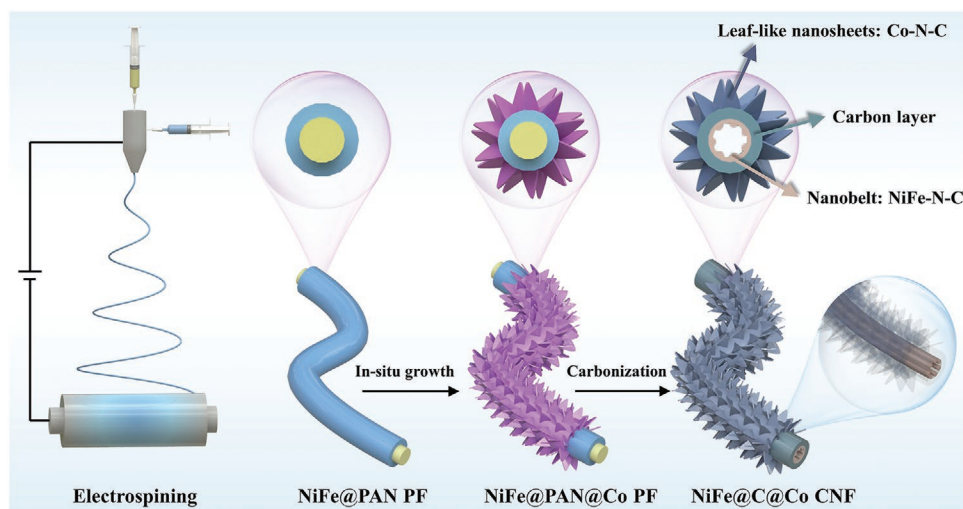


Figure 1. Schematic illustration of the synthesized process of NiFe@C@Co CNFs.

Different from the single needle-based electrospinning method to create a composite structure, the coaxial electrospinning enabled a core-shell structure where the inner layer with the precursors of OER electrocatalysts (NiFe) is wrapped by the outer layer polymer as the precursors for N-doped carbon. Then, the leaf-like zeolitic imidazolate frameworks (ZIF-L) were in situ grown on NiFe@PAN PF via a simple hydrothermal method, designated as NiFe@PAN@ZIF-L PF. To clearly confirm the synthesized Janus hollow structure, the reference fiber (PAN@ZIF-L polymer fiber) was synthesized using the same method in the absence of the PAN and Ni and Fe salts in the inner solution. Then, the synthesized polymer fibers were carbonized to obtain carbon nanofibers. The carbonized fibers are denoted as NiFe@C CNFs, C@Co CNFs, and NiFe@C@Co CNFs, respectively. To the best of our knowledge, this is the first report of 3D flexible Janus hollow nanofibers serving as superior selective oxygen electrocatalysts.

The morphology and nanostructure of the synthesized fibers were characterized by scanning electron microscopy and transmission electron microscopy (TEM). As shown in **Figure 2a**, the as-fabricated NiFe@PAN PFs possess uniform fibrous structures with an average diameter of 900 nm. It is well known that the electrospun nanofibers with submicrometer sized diameters had superior mechanical strength.^[34] Therefore, the as-fabricated Janus nanofibers would contribute to the mechanical durability of the catalyst layer. After the NiFe@PAN PFs were immersed into the water solution of 0.4×10^{-3} M 2-MeIM and 0.1×10^{-3} M $\text{Co}(\text{NO})_3 \cdot 6\text{H}_2\text{O}$ for 3 h, the leaf-like structure with the thickness of 40 nm derived from ZIF-L was vertically grown on the nanofibers with a highly opened structure, as shown in **Figure 2d**. After the thermal treatment in N_2 , the NiFe@PAN PFs were converted to carbon-based hollow nanofibers, as shown in **Figure 2b,c**. Note that the diameter of the fiber decreases from 900 to 500 nm, and the uniform fibers can contribute to superior flexibility (**Figure S1**, Supporting Information). Meanwhile, the ZIF-L on the carbon layer is converted into Co-N-C ORR catalysts and uniformly coated on the surface of the carbon layer with a leaf-like structure. The rough nanobelt combined with NiFe nanoparticles is tightly anchored

on the inner wall of the carbon layer as a kind of electrocatalyst, which is attributed to the decomposition of PMMA and the self-separation of the PAN and the PMMA during the electrospinning process.^[35,36] With the decomposition of PMMA, more active sites are exposed to boost catalytic performance. Due to the presence of PAN polymer in both internal and external solutions, the nanobelt has stronger bonding with a carbon layer, resisting material shedding compared with in situ grown or physical adsorption method during OER process. To confirm the formation of the nanobelt and the attachment between the nanobelt and the carbon layer, the composite nanofibers using the inner solution was generated to support these views by single needle-based electrospinning (**Figure S2e,f**, Supporting Information). The composite fibers decorated with NiFe alloy show a porous morphology. Interestingly, the diameter of the porous fiber increases from 600 to 800 nm without the confinement of the carbon layer. Mechanical stretching can improve the molecular orientation of PAN polymer,^[37] while the porous fiber lacks the mechanical stretching of the shell solution (the pumping velocity of outer solution in the coaxial electrospinning needle is 40% higher than that of the inner solution), giving rise to the porous fibers instead of aligned nanobelt structure in the NiFe CNFs. In contrast to the composite fibers, the Janus nanofibers with opened hollow structures can provide more space to improve the diffusion kinetics of hydroxide and facilitate the transportation of oxygen than the closed structure.

The TEM images in **Figure 3a**; and **Figure S3a** (Supporting Information) clearly prove the hollow feature with aligned nanobelts, which confirms that the high flow rate of the outer solution can facilitate the orientation of PAN polymer. Analysis of TEM images of NiFe@C CNFs demonstrates the metal particles are only located in the middle area, which provides sufficient evidence to support the formation of the hollow structure instead of the composite fiber (**Figure 3a**), showing the advantage of coaxial electrospinning technology. Considering that the NiFe alloy is in the innermost layer, it is difficult to characterize nanostructures of NiFe alloy. The NiFe@C CNFs were used to characterize the crystalline structure and element distribution of NiFe alloy. The image in **Figure 3d** shows that the carbonized

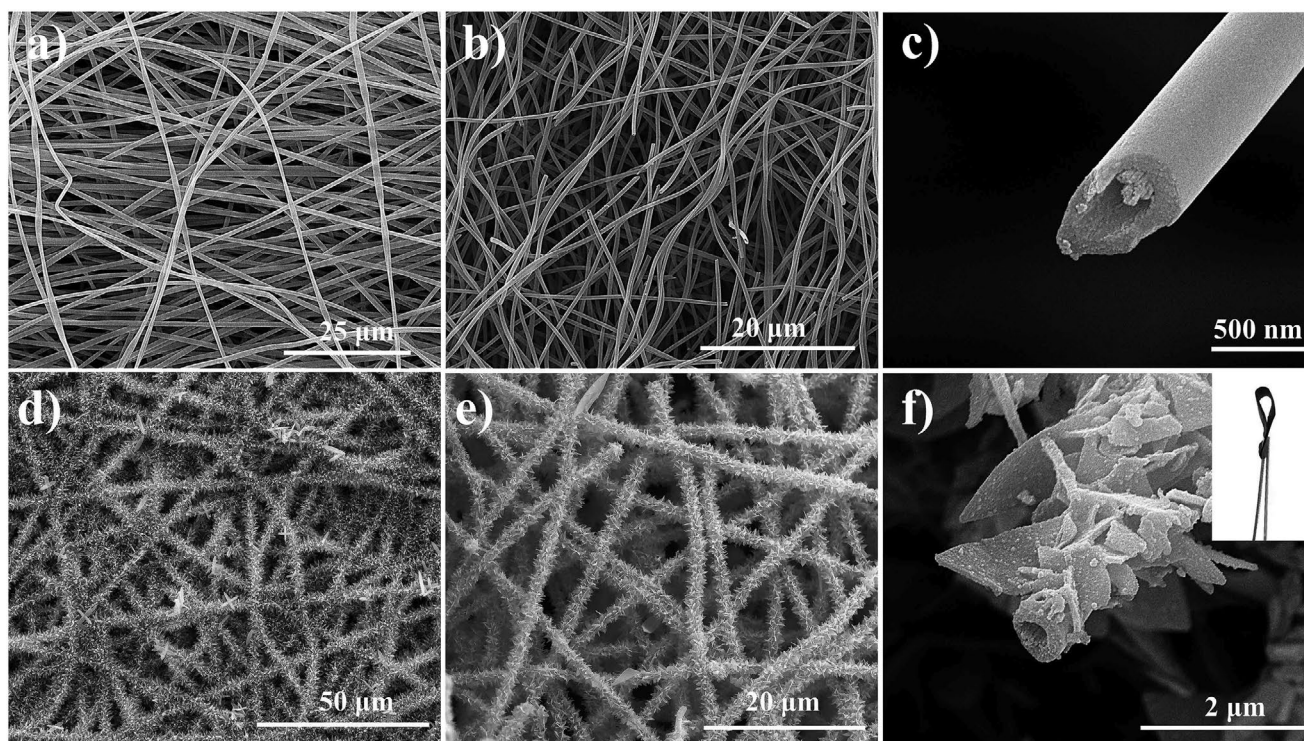


Figure 2. SEM images of a) electrospun NiFe@PAN@ZIF-L PFs, b,c) NiFe@C CNFs, d) NiFe@PAN@Co PFs, e,f) NiFe@C@Co CNFs.

ZIF-L are uniformly coated on fibers, and the Co carbon nanocatalysts derived from ZIF-L are only grown on the outer layer. The NiFe@C@Co CNFs have been decorated with numerous nanoparticles with a diameter from 15 to 50 nm (Figure S3, Supporting Information), and the smaller nanoparticles can be found in Figure S4 (Supporting Information). As shown in the HRTEM images in Figure 3b,e, the Co and NiFe nanoparticles are encapsulated by onion-like graphitic layers.^[4,38] The lattice fringes with an interplanar spacing of 0.206 nm correspond to the NiFe alloy (111) plane. The selected area electron diffraction images display the diffraction rings of NiFe on (111) (200). The diffraction spots of NiFe ($d = 0.178$ nm) are near the (101) ring of carbon, indicating NiFe nanoparticles are warped by the graphitic carbon (Figure S5a, Supporting Information). Similar results can be seen in Figure S5b (Supporting Information), which confirms Co nanoparticles are encapsulated in the graphitic carbon.^[4] The crystalline phase of the NiFe@C@Co CNFs is also confirmed by X-ray diffraction (XRD), as shown in Figure 4a. It can be observed that the peak of NiFe alloy is consistent with metallic NiFe alloy (PDF#03-4102), and the peaks of the converted ZIF-L are consistent with metallic Co (PDF#89-4307). Such graphene-coated nanoparticles endow good stability for oxygen catalysts in alkaline solutions.^[38] The elemental mapping further identifies the homogeneous dispersion of numerous elements, including C, N, Co in the outer layer and Ni, Fe, C, N in the inner layer. This homogeneity of the elements is attributed to the uniform growth of the ZIF-L and the homogeneous dispersion of metal salt in the inner solution.

The pore size and surface area of NiFe@C@Co CNFs and reference samples were characterized by N_2 adsorption and desorption isotherms (Figure 4b). The obvious hysteresis loops

of type-IV indicate the coexist of the micropores and mesopores in the fibers. Based on the Brunauer–Emmett–Teller (BET) analysis, the surface area of C@Co CNFs is $348 \text{ m}^2 \text{ g}^{-1}$, larger than that of NiFe@C CNFs ($98 \text{ m}^2 \text{ g}^{-1}$) and NiFe@C@Co CNFs ($209 \text{ m}^2 \text{ g}^{-1}$). Such porous structure with high surface area and opened hollow tube can accelerate mass transfer and enlarge the contact area between the catalyst, oxygen, and electrolyte for high electrochemical performance.^[33,39,40]

X-ray photoelectron spectroscopy (XPS) was employed to identify the surface chemistry and the binding states of various elements in NiFe@C@Co CNFs. The survey spectra indicate that there are C, N, Co, Fe, and Ni species in NiFe@C@Co CNFs; C, N, Ni, and Fe in NiFe@C CNFs; C, N, and Co in C@Co CNFs (Figure S6a, Supporting Information). As shown in Figure 4c–f; and Figure S6b (Supporting Information), the peaks of the C 1s locate at C–C/C=C (284.8 eV), C=N (285.7 eV), and C=O (288.6 eV) bonds, indicating the N element has been successfully doped into the carbon framework.^[39] The fine scan N 1s spectra can be deconvoluted into four typical peaks at 398.6, 399.6, 401.3, and 402.3 eV, corresponding to pyridinic-N, pyrrolic-N, graphitic-N, and oxidized-N, respectively.^[41,42] Pyridinic and pyrrolic N can act as metal coordination sites to form metal-N structure due to their lone-pair electron,^[43] and both of them would be active for ORR process.^[41] Graphitic N reveals that the high graphitization degree of the fibers and enhanced the electrical conductivity owing to the electronegativity difference between C and N. The Co 2p spectra of NiFe@C@Co CNFs shows the metallic state of Co (778.6 eV for $2p_{3/2}$ and 794 eV for $2p_{1/2}$) and Co–N species (780.9 eV for $2p_{3/2}$ and 796.8 eV for $2p_{1/2}$) with Co satellite peaks (785.3 and 802.8 eV).^[40,44] In comparison with the

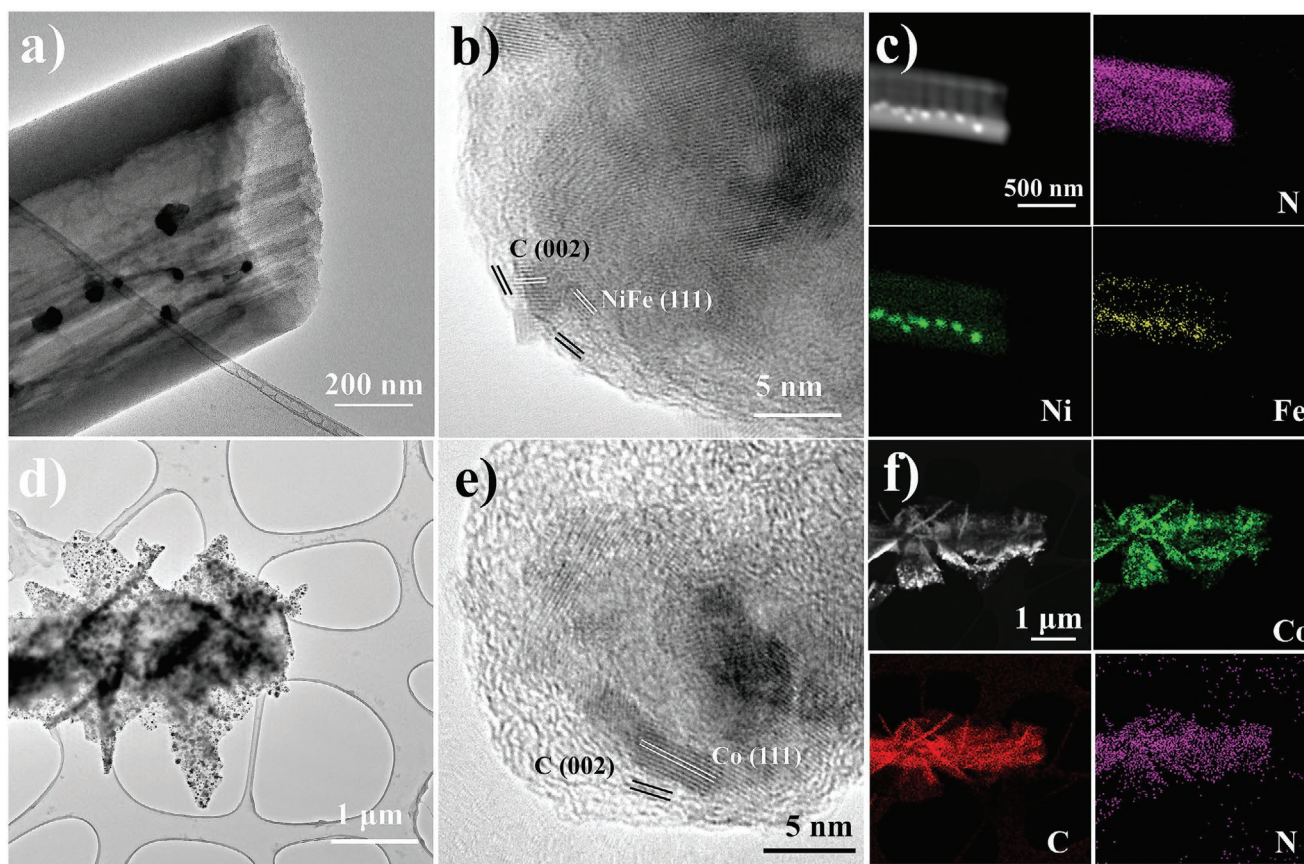


Figure 3. a,b) TEM images, c) STEM image and corresponding element mapping images of NiFe@C CNFs. d,e) TEM images, f) STEM image and corresponding element mapping images of NiFe@C@Co CNFs.

spectra of C@Co CNFs, there is no shift in the binding energy of metallic Co in NiFe@C@Co CNFs, which indicates the lack of electronic interaction between Co and Fe or Ni, further demonstrating the formation of Janus hollow fibers. The Fe 2p spectra indicate the NiFe@C@Co CNFs have metallic state of Fe (770.4 eV for 2p_{3/2} and 720.6 eV for 2p_{1/2}) and Fe–N species (711.8 eV for 2p_{3/2} and 724.2 eV for 2p_{1/2}) with Fe satellite peaks (716.2 and 729.4 eV). Similarly, the Ni 2p spectra shows the presence of metallic state of Ni (853 eV for 2p_{3/2} and 870.2 eV for 2p_{1/2}) and Ni–N species (855.3 eV for 2p_{3/2} and 873.1 eV for 2p_{1/2}) with Ni satellite peaks (861.2 and 880 eV).^[39,45–47] Compared with the NiFe@C CNFs, the unchanged binding energy of metallic Fe and Ni in NiFe@C@Co CNFs further reveal the formation of Janus hollow fibers instead of composite fibers. On the other hand, compared with Ni@C CNFs, the binding energy of metallic Ni in NiFe@C CNF is shifted toward the low energy direction, further confirming the existence of electronic interaction between Ni and Fe and the formation of NiFe alloy (Figure S6c, Supporting Information).

According to previous reports, Co–N was the active site for ORR, while the Co–N showed the sluggish kinetics of OER. The NiFe–N enabled the high catalytic activity for OER while showing limited ORR performance.^[2] To further evaluate the advantages of the Janus hollow structure, the NiFe@C@Co CNFs are used as a bifunctional electrocatalyst in Zn–air batteries. The electrocatalytic activity of the obtained fibers was

first assessed with cyclic voltammetry (CV) and Linear sweep voltammetry (LSV) with a scan rate of 5 mV s⁻¹. As shown in Figure 5a, the NiFe@C@Co and C@Co CNFs display the obvious cathodic peak at 0.9 V, which is more positive than that of Pt/C (0.89 V), while the NiFe@C CNFs show a weak cathodic peak at 0.78 V, suggesting the Co–N–C structure possesses good activity for ORR in alkaline medium. Rotating disk electrode (RDE) voltammetry of various catalysts at a rotation rate of 1600 rpm was employed to confirm this result. Onset potential E_p and half-wave potential $E_{1/2}$ (Figure 5b) are observed for NiFe@C@Co CNFs ($E_p = 0.94$ V and $E_{1/2} = 0.87$ V), C@Co CNFs ($E_p = 0.94$ V and $E_{1/2} = 0.87$ V), NiFe@C CNFs ($E_p = 0.85$ V and $E_{1/2} = 0.73$ V), and CNFs ($E_p = 0.78$ V and $E_{1/2} = 0.65$ V). The incorporation of Fe into Ni species contributes to the modified electronic structure of Ni atoms on the surface.^[48–50] As a result, The Fe-induced partial-charge transfer boosts the catalytic activity of NiFe@C CNFs, leading to a high half-wave potential (Figure S7, Supporting Information). On the contrary, the Ni@C CNFs and Fe@C CNFs show a low half-wave potential $E_{1/2}$ of 0.66 and 0.71 V, respectively. It is noted that the half-wave potential of NiFe@C@Co CNFs is higher than that of commercial Pt/C ($E_{1/2} = 0.85$ V). The low E_p and $E_{1/2}$ of CNFs indicate that uncoordinated pyridinic or pyrrolic nitrogen possess poor ORR electrocatalytic activity. Conversely, the excellent ORR activity of NiFe@C@Co CNFs indicates the N coordinated with metal is the active site for ORR in the synthesized

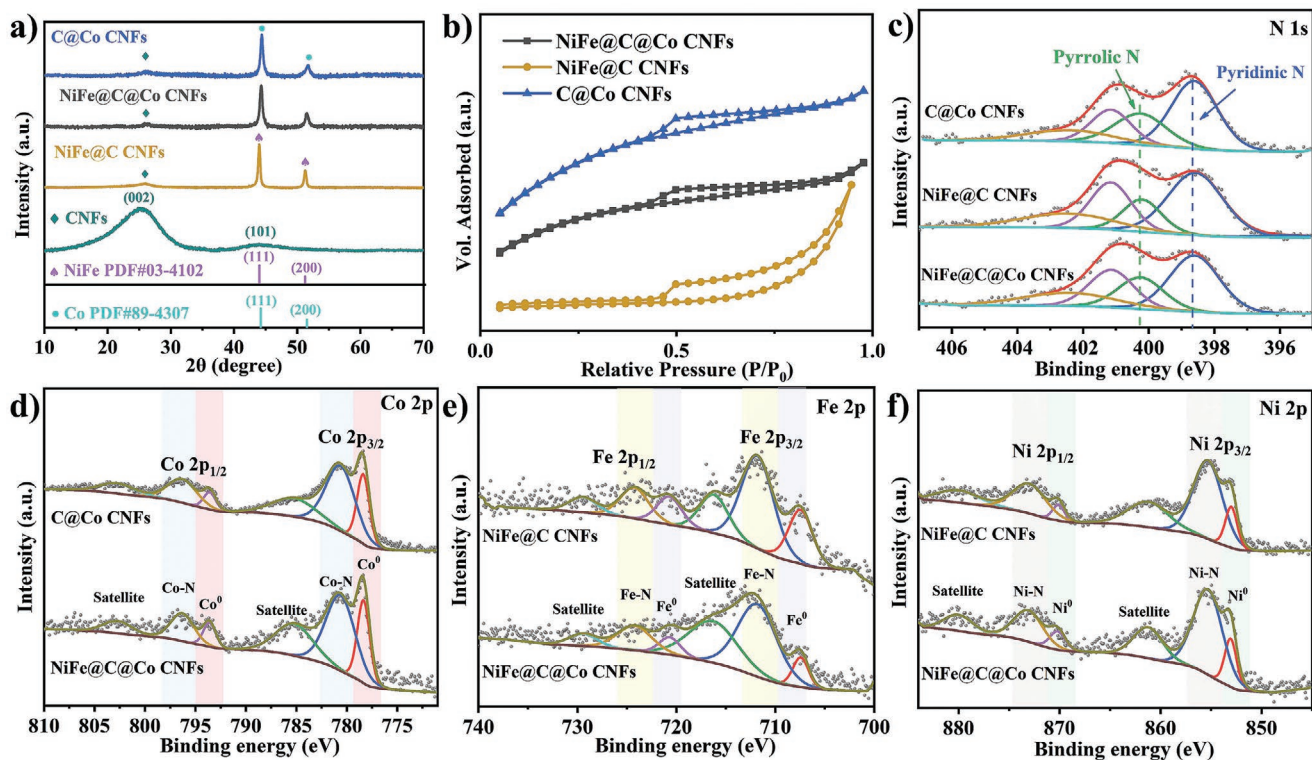


Figure 4. a) XRD patterns and b) N_2 adsorption–desorption isotherm curves of CNFs, C@Co CNFs, NiFe@C CNFs, and NiFe@C@Co CNFs. c) High-resolution N 1s spectra of C@Co CNFs, NiFe@C CNFs, and NiFe@C@Co CNFs. d) High-resolution Co 2p spectra of C@Co CNFs and NiFe@C@Co CNFs. e) High-resolution Fe 2p spectra of NiFe@C CNFs and NiFe@C@Co CNFs. f) High-resolution Ni 2p spectra of NiFe@C CNFs and NiFe@C@Co CNFs.

NiFe@C@Co electrocatalyst. Furthermore, the Tafel slopes were used to examine the catalytic kinetics for ORR. Compared to CNFs (119 $mV\ dec^{-1}$), NiFe@C CNFs (94 $mV\ dec^{-1}$), Pt/C (87 $mV\ dec^{-1}$), C@Co CNFs and NiFe@C@Co CNFs have a lower Tafel slope of 56 and 57 $mV\ dec^{-1}$, respectively. These results suggest that the Janus hollow fibers outperform other conventional catalysts in terms of ORR kinetics.^[19,21] Moreover, the Janus hollow fiber reveals a similar Tafel slope with C@Co CNFs, which proves the unchanged reaction pathway for ORR after introducing the nanobelt structure decorated with NiFe alloy, further confirming the Co–N was the active site for ORR. To evaluate the electron transfer number (n) of the catalysts, Koutecký–Levich (K–L) plots were drawn at different rotating speeds from 400 to 2500 rpm. The linearity and coincidence of K–L plots indicate that the catalysts possess the first-order reaction kinetics with respect to the dissolved oxygen concentration.^[51,52] The electron transfer number of NiFe@C@Co is about 4 at 0.3–0.8 V, which is closed to the ideal value of Pt/C ($n = 4$), showing the advantages of ZIF L-derived Janus fiber with ideal catalytic activity for ORR performance. The 4-electron mechanism is more efficient and suitable for Zn–air batteries, which will avoid the decline of the electrocatalyst activity caused by oxidation/corrosion of the carbon support,^[53] contributing to long-term stability. Besides the high activity for ORR, the durability of the NiFe@C@Co CNFs is also evaluated (Figure 5f). The NiFe@C@Co CNFs exhibit superior stability after testing for 48 h. However, the current density of the commercial Pt/C is reduced by 50% after 3.3 h. Compared with Pt/C, the superior

stability of Janus hollow fiber is attributed to the protection of onion-like graphitic layers and the 4-electron mechanism.^[12,39]

To develop bifunctional oxygen electrocatalysis, we introduced a unique carbon nanobelt decorated with NiFe alloy to catalyze OER. The polarization curves display that NiFe@C@Co CNFs have an overpotential of 336 mV to reach the current density of 10 $mA\ cm^{-2}$, which is lower than that of C@Co CNFs (410 mV) and RuO_2 (337 mV), demonstrating the high OER activity of NiFe@C@Co CNFs. Compared with benchmark RuO_2 catalysts, NiFe@C, and NiFe@C@Co CNFs exhibit superior overpotential, but the overpotential of NiFe@C@Co CNFs is lower than that of NiFe@C CNFs due to the low mass fraction of Ni and Fe. Furthermore, the Tafel slope of NiFe@C@Co CNFs is 62 $mV\ dec^{-1}$ and lower than that of the RuO_2 (85 $mV\ dec^{-1}$), C@Co CNFs (114 $mV\ dec^{-1}$), and CNFs (144 $mV\ dec^{-1}$), indicating the fastest OER kinetics of NiFe@C@Co CNFs among the obtained catalysts. Besides, the high overpotential of CNFs indicates that uncoordinated pyridinic or pyrrolic nitrogen possess poor OER activity. Hence, the difference in the activity of M–N–C should originate from the different metal centers, confirming that N coordinated with metal in the active site instead of pyridinic-N or pyrrolic-N. The result can be further supported by electrochemical impedance spectroscopy (EIS). As shown in Figure 6c, the charge-transfer resistance (R_{ct}) values are 18, 19, 20, 30, and 50 Ω for NiFe@C@Co CNFs, NiFe@C CNFs, C@Co CNFs, RuO_2 , and CNFs, respectively, which indicates the lower impedance and faster reaction kinetics of NiFe@C@Co CNFs.^[54] The electrochemical double-layer capacitance (C_{dl}) was employed

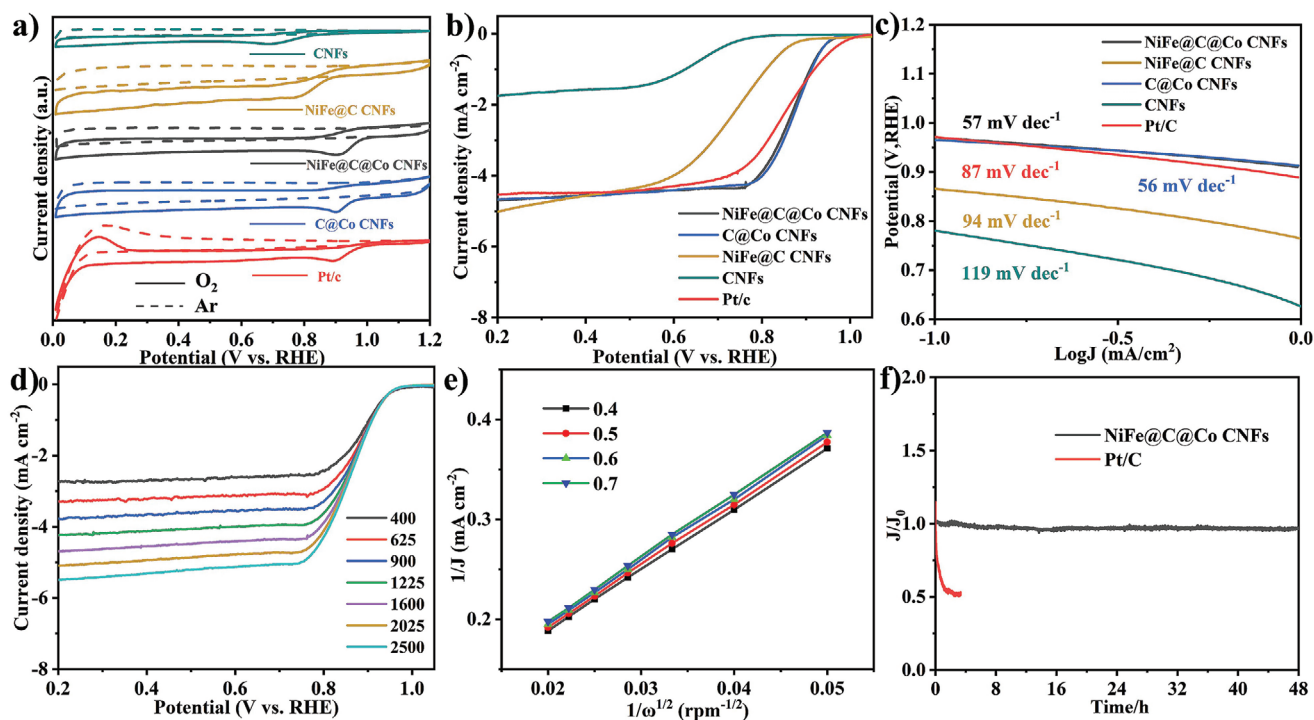


Figure 5. Electrochemical performance results of CNFs, C@Co CNFs, NiFe@C CNFs, NiFe@C@Co CNFs, and Pt/C. a) Cyclic voltammograms in 0.1 M KOH solution saturated with Ar and O₂, b) LSV polarization curves at the rotation rate of 1600 rpm, c) Tafel curves. d) LSV curves of NiFe@C@Co CNFs at different rotation rates. e) K–L plot of NiFe@C@Co CNFs at different potentials. f) Durability test result of NiFe@C@Co CNFs and Pt/C at 0.5 V (vs RHE).

to investigate the electrochemical active surface area. The calculated C_{dl} of NiFe@C@Co CNFs is 7.39 mF cm^{-2} , which is higher than that of C@Co CNFs (7.06 mF cm^{-2}), RuO₂ (3.76 mF cm^{-2}), CNFs (1.02 mF cm^{-2}), and Pt/C (0.31 mF cm^{-2}). These C_{dl} results show the NiFe@C@Co CNFs with nanobelt and leaf-like nanosheet provide more exposed active sites, which are available for the adsorption of the reactant molecules and subsequent product desorption. It is worth mentioning that the calculated C_{dl} of NiFe@C CNFs is higher than that of NiFe@C@Co CNFs. The high C_{dl} of NiFe@C CNFs is attributed to the formation of the roughness nanobelt with the decomposition of PMMA, which shows the advantages of the Janus hollow fibers with aligned nanobelt. Apart from the electrochemical activity, the electrochemical stability of NiFe@C@Co CNFs was measured in Figure 6e. Due to capillary action, the electrolyte can be sucked into the core of the Janus hollow fiber, which can significantly promote the infiltrating of the electrolyte for more catalytic sites to react with OH⁻ during OER. As a result, the initial current density of NiFe@C@Co CNFs increases with time, and the measured peak density is up to 106%. Then, the current density decreases by 15% after testing for 48 h. In contrast, the benchmark RuO₂ is reduced by 75% after testing for 3.3 h. This result shows that NiFe@C@Co CNFs possess higher stability than commercial RuO₂. The good electrochemical stability of NiFe@C@Co CNFs can be explained as follows: i) The precursor of carbon nanobelt is PAN, which is the same as that of the carbon layer, facilitating the formation of a complete whole. This integral structure, with the absence of the distinguishable interface between the nanobelt and the carbon layer,

can prevent the Janus hollow fibers from shedding during OER process as compared with the reported bifunctional catalysts by in situ growth or physical adsorption. ii) When the size of oxygen bubbles produced by OER ultimately reaches the same order of magnitude as the inner diameter of Janus nanofibers, the growth of oxygen bubbles is limited by the confinement effect, contributing to forming the nanosized bubbles. This reduces the lifting and shearing forces of the oxygen bubbles on the nanobelt OER catalysts, thus improving the structural stability of the NiFe@C@Co CNFs. In comparison with bubbles at the electrodes blocking active sites, the nanosized bubbles could be easily released, which is available for improving the reaction area. iii) Benefiting from the Janus hollow structure, the carbon nanobelts decorated with NiFe alloy and leaf-like Co–N nanosheets are located on the inner wall and outer wall of the carbon layer, respectively. The oxygen bubbles produced by NiFe alloy electrocatalysts are constrained by the carbon layer, which reduces the force acting on the leak-like Co–N nanosheets, contributing to maintaining the NiFe@C@Co CNFs interface during the oxidation progress. The OER activity of the synthesized electrocatalysts was also examined in 0.1 M KOH (Figure S8, Supporting Information). The NiFe@C@Co CNFs display a low overpotential of 370 mV to reach the current density of 10 mA cm^{-2} , which is close to the commercial RuO₂ (369 mV), demonstrating its excellent OER activity. Moreover, the OER/ORR bifunctional activity was further evaluated through the potential gap (ΔE) between the ORR half-wave potential $E_{1/2}$ and the OER potential at 10 mA cm^{-2} in 0.1 M KOH. A small ΔE value indicates superior bifunctional

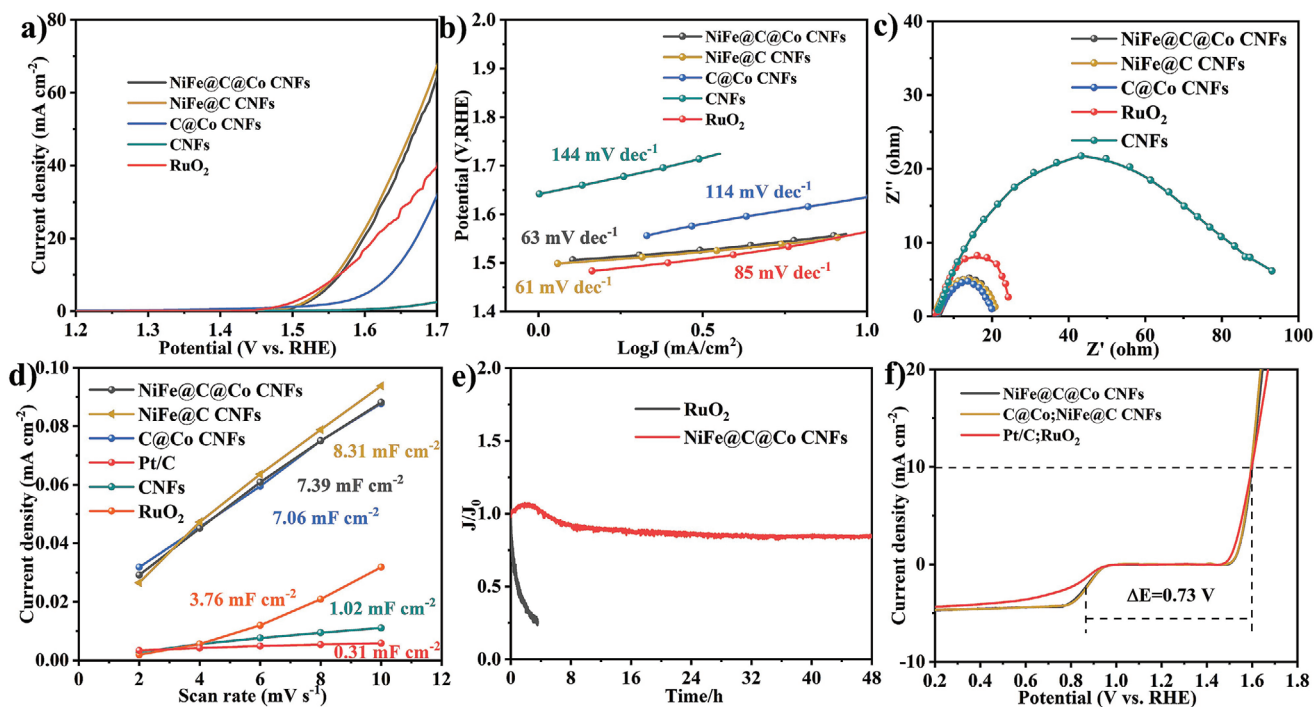


Figure 6. Electrochemical performance results of CNFs, C@Co CNFs, NiFe@C CNFs, NiFe@C@Co CNFs, and RuO₂. a) LSV polarization curves, b) Tafel curves. c) Nyquist plots. d) Electrochemical active surface area plots. e) Durability test result of NiFe@C@Co CNFs and RuO₂ at 10 mA cm⁻². f) Overall polarization curves of NiFe@C@Co CNFs, Pt/C, RuO₂, C@Co CNFs, and NiFe@C CNFs in 0.1 M KOH.

activity and less efficiency loss.^[51] As shown in Figure 6f, the NiFe@C@Co CNFs with a low ΔE value of 0.73 V exhibit excellent bifunctional electrocatalytic activity, which is better than the mixed commercial noble catalyst with 20% Pt/C and RuO₂ ($\Delta E = 0.749$ V). As shown in Table S1 (Supporting Information), the NiFe@C@Co CNFs developed in this work demonstrate a much higher efficiency as compared to the bifunctional electrocatalysts reported in literature.

To investigate the practical application of the obtained bifunctional catalysts, we assembled a liquid rechargeable Zn–air battery. As shown in Figure 7a, the Janus NiFe@C@Co CNFs exhibit an open-circuit voltage of 1.44 V, higher than that of Pt/C. Compared with the charge and discharge polarization curves of Pt/C, the NiFe@C@Co CNFs display a lower potential gap (e.g., 1.26 and 1.79 V at 10 mA cm⁻² for NiFe@C@Co CNFs, 1.16 and 1.76 V for Pt/C). This result implies a superior charge–discharge ability, which is consistent with the catalytic performance observed in the three-electrode configuration. The NiFe@C@Co CNFs have a peak power density of 130 mW cm⁻², higher than that of Pt/C (maximum 75 mW cm⁻²). Moreover, the Zn–air battery with the different catalysts was discharged at 5 mA cm⁻². The Janus NiFe@C@Co CNFs also exhibit a larger discharge specific capacity of 694 mAh g⁻¹ with a corresponding energy density of 874 Wh kg⁻¹ (when normalized to the mass of consumed Zn), outperforming the benchmark Pt/C (545 mAh g⁻¹ and 632 Wh kg⁻¹). A voltage drop originates from the carbonization of KOH solution with CO₂ in the atmosphere, leading to the decrease of electrolyte conductivity and hydroxyl ion concentration.^[51] As a demonstration, two Zn–air batteries connected in series can sufficiently power

a light emitting diode (LED) screen (Figure 7f). To further investigate the rechargeability and stability of the Zn–air battery, the cyclic galvanostatic charge–discharge measurements was employed at a current density of 5 mA cm⁻² with a duration of 20 min per cycle. The charge and discharge potential gap of NiFe@C@Co CNFs (0.77 V) is lower than that of Pt/C (0.88 V). After the charge and discharge cycling for 67 h, only a negligible deterioration of the obtained bifunctional catalyst can be observed in Figure 7e, demonstrating that the Janus NiFe@C@Co CNFs have superior charge and discharge stability. The synthesized NiFe@C@Co CNFs endow the Zn–air battery with higher energy density and cycling stability than Zn–air batteries with state-of-art bifunctional electrocatalysts (Table S2, Supporting Information). However, the performance of the benchmark catalyst combined with Pt/C and RuO₂ decreases rapidly after 33 h. In addition, SEM images (Figure S10, Supporting Information) indicate that the Janus hollow structure of NiFe@C@Co CNFs remains unchanged after long-term charge–discharge cycling, where carbon nanobelts are still located on the inner wall of the carbon layer, and leaf-like nanosheets are anchored on the outer wall of the carbon layer, demonstrating its structural stability. The XRD pattern (Figure S11, Supporting Information) also shows that the crystalline phase of NiFe@C@Co CNFs is stable after charge–discharge cycling. While the byproduct K₂CO₃ was observed on the air cathode in Figures S10 and S11 (Supporting Information), generated by the reaction between KOH and CO₂ in air,^[55,56] which is another obstacle to be solved in the research of Zn–air battery. With the above-mentioned results, it can be concluded that NiFe@C@Co CNF is a highly efficient and stable air cathode

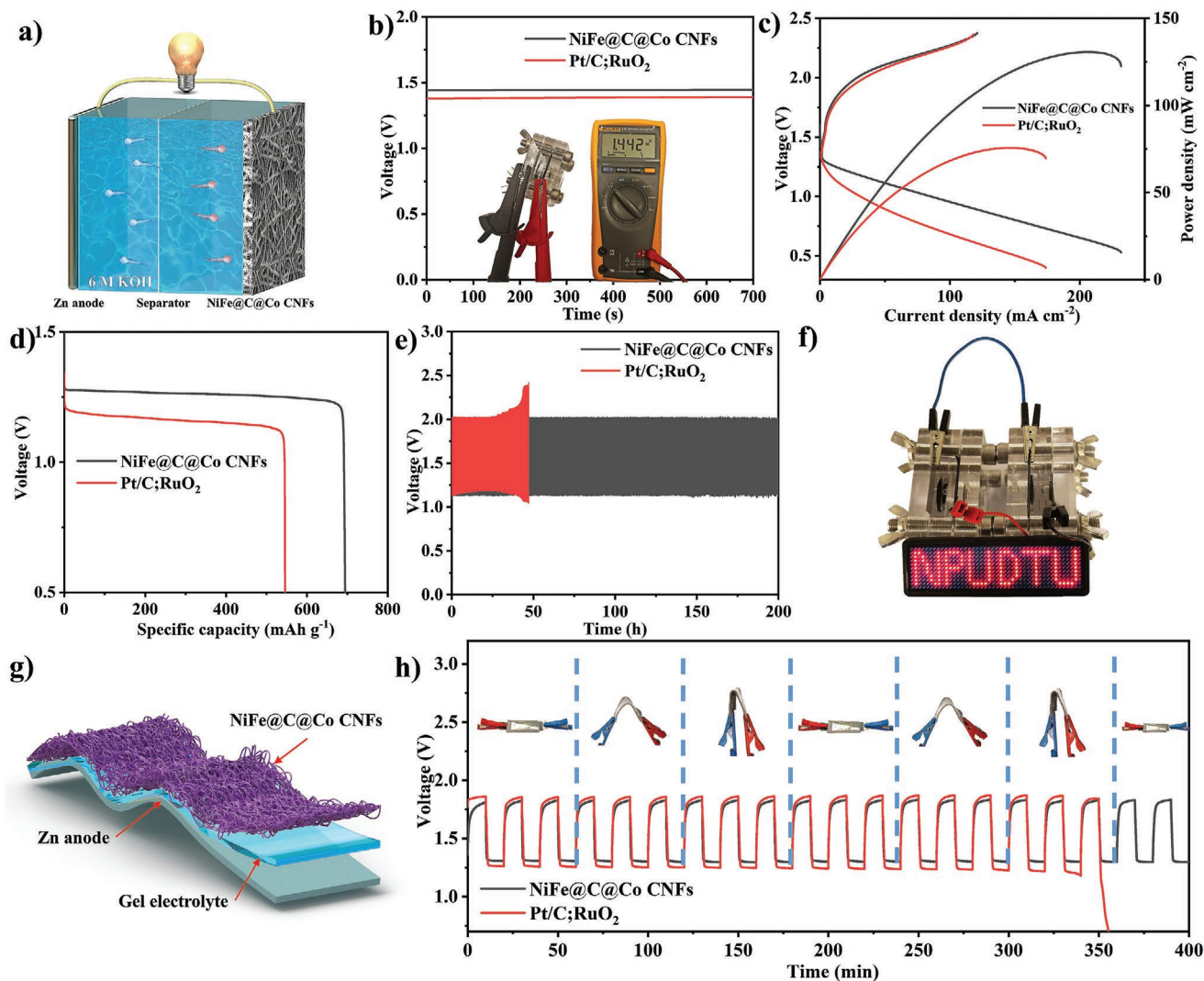


Figure 7. Electrochemical performance of the NiFe@C@Co CNFs and commercial Pt/C+RuO₂ mixture catalysts in a Zn-air battery. a) Schematic illustration of the rechargeable liquid-state Zinc-air battery. b) Open-circuit potential plots. c) Charge and discharge polarization curves and power density plots. d) Discharge curves at a constant current density of 5 mA cm⁻². e) Galvanostatic charge-discharge cycling curves at 5 mA cm⁻². f) The photo of a LED screen powered by two NiFe@C@Co CNFs-based Zn-air batteries in series. g) Schematic illustration of a flexible solid-state Zinc-air battery. h) Galvanostatic charge-discharge cycling curves at 5 mA cm⁻², and the insert is the photo of the solid battery with different bending angles.

that benefits from the unique Janus-like hollow structure. First, the hollow structure with a high surface area provides sufficient active sites and accelerates mass transfer. Moreover, the onion-like graphitic layer enhances the electrical conductivity and prevents direct contact with the electrolyte and metal nanoparticles. Such encapsulated structure contributes to long-term stability. The powder-based electrocatalysts assembled with polymeric binders suffer from reduced active sites and enlarged interfacial impedance with poor stability.^[52] The self-standing NiFe@C@Co CNFs with highly opened structures can provide more active sites and improve the energy density as well as the durability of Zn-air batteries. Driven by the increasing demand for portable and wearable devices, a flexible solid-state Zn-air battery was also fabricated using NiFe@C@Co CNFs as the air cathode, Zn foil as the anode with poly(vinyl alcohol) (PVA)-KOH electrolyte. The solid-state battery exhibits a stable cycle

life at different bending angles (Figure 7h), while the commercial catalyst combined with Pt/C and RuO₂ decreases rapidly after 350 min, confirming the excellent flexibility.

3. Conclusion

In summary, we developed a novel strategy for constructing Janus-like bifunctional electrocatalysts by using 3D flexible core-shell hollow fiber as a template, with N-doped nanobelt (Ni-Fe-N-C) and leaf-like nanosheets (Co-N-C) separately located on the inner and outer walls of the hollow carbon fibers, respectively. Benefiting from the unique Janus-like hollow structure, the synthesized NiFe@C@Co CNFs not only possess an opened hollow structure with a high surface area (209 m² g⁻¹), providing efficient active sites with a short ion-diffusion path

but also exhibit excellent bifunctional catalytic performance for ORR and OER in an alkaline electrolyte, which outperforms the state-of-the-art Pt/C and RuO₂ catalysts. Furthermore, the synthesized Janus nanofibers have superior mechanical flexibility, and it can be used as a high-performance cathode for flexible quasisolid Zn–air batteries. The rechargeable Zn–air batteries using bifunctional NiFe@C@Co CNFs deliver a large open-circuit voltage of 1.44 V, high power density (130 mW cm⁻²), energy density (874 Wh kg⁻¹) and long-term durability. This work offers an alternative approach to rationally designing bifunctional materials with excellent ORR and OER electrochemical performance to address the critical challenges in zinc–air batteries.

4. Experimental Section

Materials: PAN (*M_w* = 150 000), PMMA (*M_w* = 350 000), 2-methylimidazole (2-MeIm), nickel(II) acetate, iron(III) acetylacetonate, zinc acetate, PVA, 20% Pt/C, and RuO₂ were purchased from Sigma-Aldrich. *N,N*-dimethylacetamide (DMAC), potassium hydroxide (KOH), and cobalt(II) nitrate hexahydrate were obtained from Alfa Aesar.

Synthesis of Core–Shell Polymer Nanofiber: The core–shell nanofiber was fabricated by the coaxial electrospinning technique. The coaxial needle was homemade, which comprised of a 17-gauge outer needle and a coaxially placed 21-gauge needle. Typically, Ni(Ac)₂ (0.2 g), Fe(AcAc)₃ (0.2 g), PAN (0.4 g), and PMMA (1.6 g) were dissolved in 15 mL DMAC to obtain the inner solution after stirring for 24 h (solution A). 1.8 g of PAN was directly dissolved in 10 mL DMAC to obtain the outer solution with stirring for 12 h (solution B). The precursor solution A and B transferred in two 10 mL syringes were pumped by the two separate injection parts for coaxial electrospinning. The optimized core and shell flow rate to achieve a steady Taylor cone was 0.5 and 0.2 mL h⁻¹, respectively. The electrospinning voltage and distance were set to be 15 kV and 15 cm, respectively. The core–shell fibers were electrospun on a rotary drum with an aluminum foil at 500 rpm. In the process, the temperature and relative humidity were set as 25 °C and 25%, respectively, which was controlled by the NS Air Conditioning Unit (Elmarco, NS AC 150). Then, the as-fabricated fibers were dried at 60 °C overnight to move the residual solvent.

Synthesis of Janus-Like Carbon Nanofiber: Two types of solution were prepared by dissolving the 0.65 g 2-MeIm and 0.36 g Cobalt(II) nitrate hexahydrate in 20 mL DI water, respectively. Then, the cobalt nitrate solution was quickly added into the 2-MeIm solution and string for 30 s at room temperature. Then, a piece of as-fabricated core–shell polymer fibers was immersed into the purple solution. After 3 h for fully infiltrating fibers, the ZIF L was in situ grown on the polymer fiber surface. The products were washed with water 3 times and dried at 60 °C overnight. The synthesized Janus polymer nanofibers were stabilized at 230 °C for 2 h in an air atmosphere (heating rate was 1 °C min⁻¹ from ambient temperature). Finally, the products were carbonized at 800 °C for 2 h under N₂ atmosphere with a heating rate of 5 °C min⁻¹ to form Janus-like hollow carbon fiber.

Catalyst Characterizations: The morphology of the as-obtained fibers was examined using a field-emission scanning electron microscope operated at 15 kV (SEM, Quanta FEG 200), and TEM (Tecnai T20 G2) operated at 200 kV with energy-dispersive X-ray spectroscopy (EDS). The crystal structure of the synthesized fibers was characterized by XRD (Rikagu miniflex) using Cu Kα radiation (λ = 1.541 Å). The nitrogen desorption–absorption isotherm were carried out, and the specific surface area was obtained based on (Brunauer–Emmett–Teller) BET method (Micromeritics, Gemini 2375). The valence states were detected using X-ray photoelectron spectroscopy (XPS, Nexsa, Al as the Target).

Electrochemical Measurements: The OER and ORR catalytic performance were performed on a three-electrode cell (Biologic SP300) at room temperature. The L-shaped glass carbon electrode (RDE, 0.196 cm²) modified with catalysts served as the working electrode, and

a saturated calomel electrode was used as the reference electrode for OER. A carbon rod and an Ag/AgCl electrode were employed as the counter and reference electrode for ORR, respectively. The catalyst ink was prepared by adding 5 mg ground catalyst to 1 mL 1:1 v/v water/ethanol solvent containing Nafion solution (5 wt%, 30 μL). The obtained ink was ultrasonically dispersed for 1 h. Then 10 μL ink was coated on the electrode and dried at the ambient environment to obtain a catalyst loading of about 0.255 mg cm⁻². For comparison, commercial Pt/C and RuO₂ with the same mass loading were prepared. All the potential values were transferred regarding a standard reversible hydrogen electrode (RHE) according to the equation: $E_{\text{RHE}} = E_{\text{Ag/AgCl}} + 0.059 * \text{pH} + 0.21 \text{ V}$ or $E_{\text{RHE}} = E_{\text{Hg/HgO}} + 0.059 * \text{pH} + 0.098 \text{ V}$.

ORR Tests: The CV was measured in 0.1 M KOH solution saturated with Ar or O₂ with a scan rate of 5 mV s⁻¹. LSV was performed with rotation speeds from 400 to 2500 rpm at a scan rate of 5 mV s⁻¹. The chronoamperometric curve was carried with a rotation speed of 1600 rpm at 0.5 V (vs RHE) for 12 000 s.

Tafel slopes were calculated following the Tafel equation

$$\eta = b \log(j) + a \quad (1)$$

Where η , b , and j are the potentials, Tafel slope and current density, respectively.

The K–L plots could be calculated to obtain the electron transfer number according to the equation

$$\frac{1}{j} = \frac{1}{j_L} + \frac{1}{j_k} = \frac{1}{B\omega^{1/2}} + \frac{1}{j_k} \quad (2)$$

$$B = 0.2nFC_0D_0^{2/3}v^{1/6} \quad (3)$$

Where j is the current density, j_L is the limiting diffusion current density, and j_k is the kinetic density. ω is the rotation speed (rpm), n is the electron transfer number. F is the Faraday constant (96 485 C mol⁻¹), C_0 is the bulk concentration of O₂ (1.2 × 10⁻⁶ mol cm⁻³), D_0 is the diffusion coefficient of O₂ (1.9 × 10⁻⁵ cm² s⁻¹), and v is the kinematic viscosity of the electrolyte (0.01 cm² s⁻¹).

OER Tests: The OER performance was tested in 1 M KOH saturated with Ar. The linear sweep voltammetry was performed at a scan rate of 5 mV s⁻¹ with 85% iR correct. The chronoamperometric curve was carried out with a current density of 10 mA cm⁻² for 12 000 s. The electrochemical impedance spectra (EIS) were measured with an amplitude of 5 mV and frequency range from 0.01 Hz to 100 kHz.

C_{dl} values were determined by using CV in the potential range between 1.045 and 1.085 versus RHE with various scan rates of 2, 4, 6, 8, and 10 mV s⁻¹. By plotting the difference of current density (j) between the anodic and cathodic sweeps ($j_{\text{anodic}} - j_{\text{cathodic}}$) at 1.06 V versus RHE as a function of the scan rate, the slopes are calculated as the C_{dl} .

Zn–Air Battery Assembly: The Zn–air battery performance was examined with a homemade Zn–air cell. The air cathode was comprised of hydrophilic carbon paper with a catalyst layer and a gas-diffusion layer. The NiFe@C@Co Janus nanofibers were used as the catalyst layer. A polished zinc foil and 6 M KOH solution containing 0.2 M zinc acetate were used as the anode and electrolyte, respectively. All Zn–air batteries were examined by (Biologic SP300) at ambient conditions. The galvanostatic discharge–charge cycling was recorded at 5 mA cm⁻². Each discharge and charge period was set to be 10 min.

Flexible Quasisolid-State Zn–Air Battery Assembly: The NiFe@C@Co Janus nanofibers were used as air cathode. The polymeric hydrogel electrolyte was prepared as follows: 1g PVA powder was dissolved in 10 mL deionized water at 80 °C under magnetic stirring to obtain a transparent solution. Then 1 mL of 18 M KOH filled with 0.2 M zinc acetate was added into the solution for 40 min. A small portion of the solution was transferred into the acrylic mold to form a thin film at room temperature. Finally, the flexible quasisolid-state Zn–air battery was assembled with the as-prepared Janus membrane and zinc foil on the two sides of PVA gel, and the pressed Ni foam was used as a current collector next to the air electrode.

Supporting Information

Supporting Information is available from the Wiley Online Library or from the author.

Acknowledgements

X.C. and J.P. contributed equally to this work. W.Z. would like to thank the research funding support from Danish Research Council (Grant No. 8022-00237B). X.C. would like to thank the funding support from the Chinese Science Council for his stay at DTU.

Conflict of Interest

The authors declare no conflict of interest.

Data Availability Statement

The data that support the findings of this study are available from the corresponding author upon reasonable request.

Keywords

electrospinning, hollow nanofibers, Janus structures, metal–organic frameworks, oxygen electrocatalysts, zn–air batteries

Received: January 26, 2022

Revised: February 24, 2022

Published online: March 18, 2022

- [1] H. Shang, X. Zhou, J. Dong, A. Li, X. Zhao, Q. Liu, Y. Lin, J. Pei, Z. Li, Z. Jiang, *Nat. Commun.* **2020**, *11*, 1.
- [2] X. Cui, P. Ren, D. Deng, J. Deng, X. Bao, *Energy Environ. Sci.* **2016**, *9*, 123.
- [3] J. Pu, Q. Cao, Y. Gao, J. Yang, D. Cai, X. Chen, X. Tang, G. Fu, Z. Pan, C. Guan, *J. Mater. Chem. A* **2021**, *9*, 17292.
- [4] C. Guan, A. Sumboja, H. Wu, W. Ren, X. Liu, H. Zhang, Z. Liu, C. Cheng, S. J. Pennycook, J. Wang, *Adv. Mater.* **2017**, *29*, 1704117.
- [5] J. Chen, H. Li, C. Fan, Q. Meng, Y. Tang, X. Qiu, G. Fu, T. Ma, *Adv. Mater.* **2020**, *32*, 2003134.
- [6] D. Liu, B. Wang, H. Li, S. Huang, M. Liu, J. Wang, Q. Wang, J. Zhang, Y. Zhao, *Nano Energy* **2019**, *58*, 277.
- [7] Z. Liu, B. Tang, X. Gu, H. Liu, L. Feng, *Chem. Eng. J.* **2020**, *395*, 125170.
- [8] X. Han, X. Ling, D. Yu, D. Xie, L. Li, S. Peng, C. Zhong, N. Zhao, Y. Deng, W. Hu, *Adv. Mater.* **2019**, *31*, 1905622.
- [9] P. Chen, K. Xu, Z. Fang, Y. Tong, J. Wu, X. Lu, X. Peng, H. Ding, C. Wu, Y. Xie, *Angew. Chem.* **2015**, *127*, 14923.
- [10] S. Y. Lim, S. Martin, G. Gao, Y. Dou, S. B. Simonsen, J. O. Jensen, Q. Li, K. Norrman, S. Jing, W. Zhang, *Adv. Funct. Mater.* **2021**, *31*, 2006771.
- [11] J. Zhang, Y. Zhao, C. Chen, Y.-C. Huang, C.-L. Dong, C.-J. Chen, R.-S. Liu, C. Wang, K. Yan, Y. Li, *J. Am. Chem. Soc.* **2019**, *141*, 20118.
- [12] W. Wan, S. Wei, J. Li, C. A. Triana, Y. Zhou, G. R. Patzke, *J. Mater. Chem. A* **2019**, *7*, 15145.
- [13] J. Deng, D. Deng, X. Bao, *Adv. Mater.* **2017**, *29*, 1606967.
- [14] D. Deng, L. Yu, X. Chen, G. Wang, L. Jin, X. Pan, J. Deng, G. Sun, X. Bao, *Angew. Chem.* **2013**, *125*, 389.
- [15] M. X. Chen, M. Zhu, M. Zuo, S. Q. Chu, J. Zhang, Y. Wu, H. W. Liang, X. Feng, *Angew. Chem.* **2020**, *132*, 1644.
- [16] C. Tang, B. Wang, H. F. Wang, Q. Zhang, *Adv. Mater.* **2017**, *29*, 1703185.
- [17] X. Sun, C. Wang, Y. Gong, L. Gu, Q. Chen, Y. Yu, *Small* **2018**, *14*, 1802218.
- [18] Q. Wang, L. Shang, R. Shi, X. Zhang, Y. Zhao, G. I. Waterhouse, L. Z. Wu, C. H. Tung, T. Zhang, *Adv. Energy Mater.* **2017**, *7*, 1700467.
- [19] J. Wu, H. Zhou, Q. Li, M. Chen, J. Wan, N. Zhang, L. Xiong, S. Li, B. Y. Xia, G. Feng, *Adv. Energy Mater.* **2019**, *9*, 1900149.
- [20] Q. Yang, Y. Jia, F. Wei, L. Zhuang, D. Yang, J. Liu, X. Wang, S. Lin, P. Yuan, X. Yao, *Angew. Chem.* **2020**, *132*, 6178.
- [21] X. Sun, S. Sun, S. Gu, Z. Liang, J. Zhang, Y. Yang, Z. Deng, P. Wei, J. Peng, Y. Xu, *Nano Energy* **2019**, *61*, 245.
- [22] H. Lei, Z. Wang, F. Yang, X. Huang, J. Liu, Y. Liang, J. Xie, M. S. Javed, X. Lu, S. Tan, *Nano Energy* **2020**, *68*, 104293.
- [23] G. Fu, Z. Cui, Y. Chen, Y. Li, Y. Tang, J. B. Goodenough, *Adv. Energy Mater.* **2017**, *7*, 1601172.
- [24] D. Bin, B. Yang, C. Li, Y. Liu, X. Zhang, Y. Wang, Y. Xia, *ACS Appl. Mater. Interfaces* **2018**, *10*, 26178.
- [25] P. d. Gennes, *Science* **1992**, *256*, 495.
- [26] Z. Zhang, X. Y. Kong, K. Xiao, G. Xie, Q. Liu, Y. Tian, H. Zhang, J. Ma, L. Wen, L. Jiang, *Adv. Mater.* **2016**, *28*, 144.
- [27] Z. Song, W. Li, Y. Bao, W. Wang, Z. Liu, F. Han, D. Han, L. Niu, *Adv. Electron. Mater.* **2018**, *4*, 1800252.
- [28] L. Zhang, M. Cong, X. Ding, Y. Jin, F. Xu, Y. Wang, L. Chen, L. Zhang, *Angew. Chem.* **2020**, *132*, 10980.
- [29] Z. Wang, J. Ang, B. Zhang, Y. Zhang, X. Y. D. Ma, T. Yan, J. Liu, B. Che, Y. Huang, X. Lu, *Appl. Catal., B* **2019**, *254*, 26.
- [30] Y. Li, H. Li, K. Cao, T. Jin, X. Wang, H. Sun, J. Ning, Y. Wang, L. Jiao, *Energy Storage Mater.* **2018**, *12*, 44.
- [31] Y. Chen, W. Zhang, Z. Zhu, L. Zhang, J. Yang, H. Chen, B. Zheng, S. Li, W. Zhang, J. Wu, F. Huo, *J. Mater. Chem. A* **2020**, *8*, 7184.
- [32] W. Li, S. Chen, M. Zhong, C. Wang, X. Lu, *Chem. Eng. J.* **2021**, *415*, 128879.
- [33] C.-L. Zhang, J.-T. Liu, H. Li, L. Qin, F.-H. Cao, W. Zhang, *Appl. Catal., B* **2020**, *261*, 118224.
- [34] D. Papkov, N. Delpouve, L. Delbreilh, S. Araujo, T. Stockdale, S. Mamedov, K. Maleckis, Y. Zou, M. N. Andalib, E. Dargent, V. P. Dravid, M. V. Holt, C. Pellerin, Y. A. Dzenis, *ACS Nano* **2019**, *13*, 4893.
- [35] A. V. Bazilevsky, A. L. Yarin, C. M. Megaridis, *Langmuir* **2007**, *23*, 2311.
- [36] Y. Yu, L. Gu, C. Zhu, P. A. Van Aken, J. Maier, *J. Am. Chem. Soc.* **2009**, *131*, 15984.
- [37] M. Richard-Lacroix, C. Pellerin, *Macromolecules* **2013**, *46*, 9473.
- [38] L. Chong, J. Wen, J. Kubal, F. G. Sen, J. Zou, J. Greeley, M. Chan, H. Barkholtz, W. Ding, D.-J. Liu, *Science* **2018**, *362*, 1276.
- [39] Z. Li, H. He, H. Cao, S. Sun, W. Diao, D. Gao, P. Lu, S. Zhang, Z. Guo, M. Li, R. Liu, D. Ren, C. Liu, Y. Zhang, Z. Yang, J. Jiang, G. Zhang, *Appl. Catal., B* **2019**, *240*, 112.
- [40] L. Liu, X. Zhang, F. Yan, B. Geng, C. Zhu, Y. Chen, *J. Mater. Chem. A* **2020**, *8*, 18162.
- [41] H. Shen, E. Gracia-Espino, J. Ma, K. Zang, J. Luo, L. Wang, S. Gao, X. Mamat, G. Hu, T. Wagberg, *Angew. Chem.* **2017**, *129*, 13988.
- [42] C. Li, M. Wu, R. Liu, *Appl. Catal., B* **2019**, *244*, 150.
- [43] R. Liu, D. Wu, X. Feng, K. Müllen, *J. Am. Chem. Soc.* **2011**, *133*, 15221.
- [44] F. Shi, Z. Geng, K. Huang, Q. Liang, Y. Zhang, Y. Sun, J. Cao, S. Feng, *Adv. Sci.* **2018**, *5*, 1800575.
- [45] B. Li, S. P. Sasikala, D. H. Kim, J. Bak, I.-D. Kim, E. Cho, S. O. Kim, *Nano Energy* **2019**, *56*, 524.
- [46] Y. Gu, S. Chen, J. Ren, Y. A. Jia, C. Chen, S. Komarneni, D. Yang, X. Yao, *ACS Nano* **2018**, *12*, 245.

- [47] Z. Chen, R. Zheng, M. Graś, W. Wei, G. Lota, H. Chen, B.-J. Ni, *Appl. Catal., B* **2021**, *288*, 120037.
- [48] L. Trotochaud, S. L. Young, J. K. Ranney, S. W. Boettcher, *J. Am. Chem. Soc.* **2014**, *136*, 6744.
- [49] Z. Zhang, Y. Qin, M. Dou, J. Ji, F. Wang, *Nano Energy* **2016**, *30*, 426.
- [50] Y. Zhou, Y. Li, L. Zhang, L. Zhang, L. Li, J. Tian, M. Wang, J. Xu, B. Dai, Y. Li, *Chem. Eng. J.* **2020**, *394*, 124977.
- [51] Y. Zhao, Q. Lai, J. Zhu, J. Zhong, Z. Tang, Y. Luo, Y. Liang, *Small* **2018**, *14*, 1704207.
- [52] Z. Pan, H. Chen, J. Yang, Y. Ma, Q. Zhang, Z. Kou, X. Ding, Y. Pang, L. Zhang, Q. Gu, C. Yan, J. Wang, *Adv. Sci.* **2019**, *6*, 1900628.
- [53] J. Pan, Y. Y. Xu, H. Yang, Z. Dong, H. Liu, B. Y. Xia, *Adv. Sci.* **2018**, *5*, 1700691.
- [54] X. Zhu, D. Zhang, C.-J. Chen, Q. Zhang, R.-S. Liu, Z. Xia, L. Dai, R. Amal, X. Lu, *Nano Energy* **2020**, *71*, 104597.
- [55] W. Sun, M. Ma, M. Zhu, K. Xu, T. Xu, Y. Zhu, Y. Qian, *Small* **2021**, 2106604.
- [56] W. Sun, F. Wang, B. Zhang, M. Zhang, V. Küpers, X. Ji, C. Theile, P. Bieker, K. Xu, C. Wang, *Science* **2021**, *371*, 46.